Corrosion Science 163 (2020) 108293

Contents lists available at ScienceDirect

Corrosion Science

journal homepage: www.elsevier.com/locate/corsci

Analysis of combined static load and low temperature hot corrosion induced cracking in CMSX-4 at 550°C

L. Brooking[a], S. Gray[a,*], K. Dawson[b], J.R. Nicholls[a], N.J. Simms[a], J. Sumner[a], G.J. Tatlock[b]

[a] Cranfield University, College Rd, Cranfield, MK43 OAL, United Kingdom
[b] Department of Mechanical, Materials and Aerospace Engineering, School of Engineering, University of Liverpool, Liverpool L69 3GH, United Kingdom

ARTICLE INFO

Keywords:
Superalloy
Partitioning
Stress corrosion cracking
TEM
Hot corrosion

ABSTRACT

A CMSX-4 3-point bend specimen was statically loaded under hot corrosion conditions and SEM, (S)TEM and EDX techniques were used to analyse the cracking generated. Sulphur, chlorine, sodium and oxygen were found at the crack tip, and an influence of loading on the corrosion mechanism's preference to interact with either the γ or γ′ was observed. The microscopy analysis is in support of the corrosive mechanism being a combined stress and electrochemical corrosion linked with low temperature hot corrosion, where crack propagation occurs as a result of localised corrosion enhanced material degradation. High magnification EDX mapping identified W as segregating to the γ′ at room temperature.

1. Introduction

Gas turbine (GT) systems are used for a range of applications in the aerospace and power generation sectors. In addition to economic pressures to improve the efficiencies of GT systems, emissions legislation and incentives are further driving the industry to develop more efficient designs [1–3]. In response to these drivers, GT manufacturers are looking for ways to increase the turbine inlet temperatures to improve the thermodynamic efficiency of the turbine system [4]. One of the key limiting factors in achieving this is the turbine blade's material capabilities at high temperature e.g. its corrosion resistance and performance. In order to optimise the capabilities of materials and components, accurate lifing techniques are required which account for the service conditions the component is subjected to.

However, it has been observed in recent studies that static tensile loading combined with conditions consistent with those required for low temperature hot corrosion (LTHC), can lead to crack initiation and propagation not predicted by conventional fatigue or corrosion lifing models [5–7]. These findings are indicative of LTHC stress corrosion cracking (SCC) mechanism, which requires a corrosive salt deposit such as Na_2SO_4, a gaseous environment containing SO_x (SO_2 / SO_3) and a tensile loading condition. The mechanism was generated in a single crystal (SC) superalloy, and required both stress and hot corrosion conditions to be simultaneously present. Cracking occurred below the expected fatigue stress intensity threshold (K_{TH}) and without fatigue cycles, and propagated on preferential orthogonal {001} planes.

A better understanding this cracking behaviour is particularly important in lower temperature regions of GT blades which are susceptible to LTHC operating between 500–700 °C, and are additionally under tensile loading. Such conditions are often present in the under platform regions of 1st stage GT blades. 1st stage turbine blades are commonly manufactured using single crystal (SC) Ni-based superalloy systems due to their good high temperature mechanical and oxidation properties [8,9].

1.1. Stress corrosion cracking mechanisms

Previous research into environmental cracking behaviour of superalloys has largely focused on two general approaches to quantify and explain the effects of combined loading and LTHC. In the first, the effect of LTHC on increasing the rate of fatigue crack propagation, is quantified through consideration of the loading cycles to specimen failure, where a specific mechanistic explanation was not proposed [6,10–12]. The second approach is based on a mechanism of stress concentration generated by LTHC pitting, this pitting is identified as a fatigue crack nucleation accelerator [13–15]. Both these approaches would require further development to include time dependant crack propagation resulting from a LTHC SCC mechanism.

Due to the limited published work available on LTHC SCC, a wider review of SCC cracking mechanisms has been conducted. In general terms SCC can be described as the interaction between mechanical load and corrosion of a material, specifically resulting in crack initiation and

* Corresponding author.
E-mail address: s.gray@cranfield.ac.uk (S. Gray).

https://doi.org/10.1016/j.corsci.2019.108293
Received 27 March 2019; Received in revised form 11 September 2019; Accepted 16 October 2019
Available online 18 October 2019

propagation [16]. There are three corrosion mechanisms commonly attributed with SCC in both ferritic and nickel-based alloys, these are described below.

Firstly, SCC can be generated with electrochemical corrosion conditions; this has been studied in ferritic and nickel-based alloys, where corrosion was controlled through application of an electrochemical potential [17,18]. Specimens were submerged in a liquid electrolyte and an electrical potential applied across them. A mechanism has been proposed where corrosion is generated locally at the anodic region as a result of the presence of acidic metal ions [19]. Due to the localised nature of electrochemical corrosion, when combined with stress it is well documented as generating the initiation and propagation of SCC cracking [20–22].

A second, process by which SCC commonly occurs, is by stress assisted grain boundary oxidation (SAGBO) in polycrystalline materials [23–25]. It has been hypothesised that SAGBO occurs due to the formation of niobium oxides on grain boundaries in Ni-based superalloys [26]. Whilst not directly applicable to SC alloys, SAGBO is an example of stress assisting oxidation in crystalline materials, and it has additionally been found that Cl and S containing vapours can further accelerate gas phase induced SAGBO in Ni-based superalloys [27,28].

Thirdly, SCC can be generated by the active element, hydrogen; this is referred to as hydrogen embrittlement and has been reported in Ni-based alloys at temperatures between 250–430 °C [29,30]. Whilst there is no definitive mechanism for hydrogen embrittlement, it is generally considered to occur as a result of absorption or diffusion of cathodic H^+ hydrogen, achieved through a partial pressure of hydrogen generating a concentration gradient causing adsorption to occur [31,32].

Several mechanisms for hydrogen embrittlement have been proposed, these were summarised by Lynch [33], with the overall mechanism being referred to as adsorption induced dislocation emissions (AIDE). AIDE occurs as a result of both adsorbed hydrogen enhancing de-cohesion and weakening of interatomic bonds (HEDE), and hydrogen enhancing local plasticity (HELP) [34]. Hydrogen diffusion has been studied and measured in SC nickel FCC systems [35,36].

1.2. Oxidation and corrosion of superalloys

Superalloy systems are designed to form protective oxide scales which inhibit and prevent the continued oxidation of the substrate alloy. Two of the most beneficial oxides formers for superalloys to form, are chromia (chromium oxide) and alumina (aluminium oxide). It has been found that chromia formers often perform better for lower temperatures up to 700 °C and alumina at higher temperatures above 900 °C [37].

Corrosion mechanisms such as chloridation (the formation of metal chlorides) [38], and sulphidation (the formation of metal sulphides) [39,40], can facilitate/accelerate the dissolution of protective oxide scales and cause accelerated corrosion and oxidation of the alloy substrate. However, these mechanisms require the presents of Cl/S species, such species can be fluxed onto the material from a gaseous species, through solid particle deposition or both as described by F. S. Pettit and G. H. Meier [41].

LTHC is a corrosion mechanism known to effect GTs, particularly the combustion and turbine components. This mechanisms occurs as a result of the deposition of corrosive species, it is historically reported to occur between 600 °C – 800 °C [42–44]. However, recent studies have generated LTHC in CMSX-4 at temperatures as low as 575 °C [45], and stress has been credited as further lowering the temperature required for LTHC to propagate [6]. LTHC is dependent on both a deposit flux of salt species and a gas flow containing SO_x, particularly SO_3 which are required to form and maintain the liquid mixture on the material surface.

It is generally thought that LTHC corrosion occurs through the formation of a liquid deposit, which results in the dissolution of the protective oxide scale, through acidic fluxing where dissolved SO_x is the oxidising agent. It is further believed that this occurs due to an electrochemical mechanism, where corrosive oxyanion fused salts such as Na_2SO_4 are ionically conducting, establishing an electrochemical circuit [46,47]. The salt species can be acidic when high in SO_3, dissolving oxides as a cationic species, or basic when low in SO_3 as an anionic species [48].

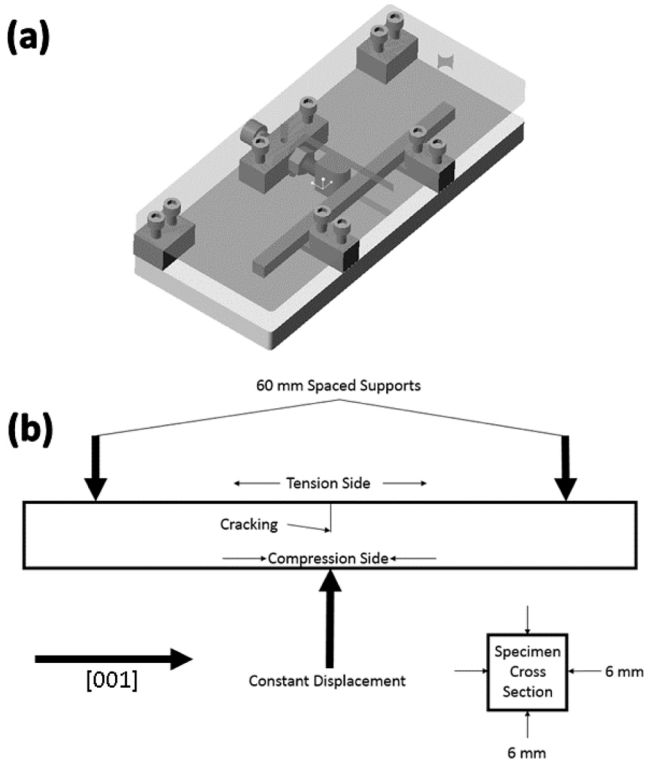

Fig. 1. (a) Specimen and jig mounting geometry (b) Three point bend test jig.

2. Experimental methods

A three point bend jig was designed for use within a hot corrosion furnace (Fig. 1a), the three point bend jig applied a constant displacement condition to a specimen (Fig. 1b). Three point bend specimens were machined with the cube planes ([001] symmetrical set) aligned as shown in Fig. 1, while the secondary orientation was not controlled. To calculate the displacement required to meet the initial load condition, BSI standard calculations were used [49], these were further validated with finite element (FE) analysis, the results of which have been previously published [5].

LTHC conditions representative of under platform turbine conditions were generated at a temperature of 550 °C using a deposit recoat methodology [50]. The deposit used was 80/20 mol% Na/K sulphate, which was deposited every 100 h of testing to maintain a flux of 5 µg/cm^2/h. A test gas of air/300 ppm SO_x was used and the test specimen was exposed for 200 h in total made up by two 100 h cycles.

To compare corrosion effects under both tension and compression, both the opposing tensile and compressively loaded sides of the specimens were coated with salt deposit equally. The remaining sides were masked off using aluminium foil in order to prevent their exposure to LTHC and more accurately control corrosion in the areas being studied.

TEM/STEM images were taken with a JEOL 2100 F microscope, fitted with an aberration corrector and operating at 200kv. EDX analysis was carried out using an EDAX Optima 60 windowless SDD detector, and the analytical data was analysed using EDAX TEAM software.

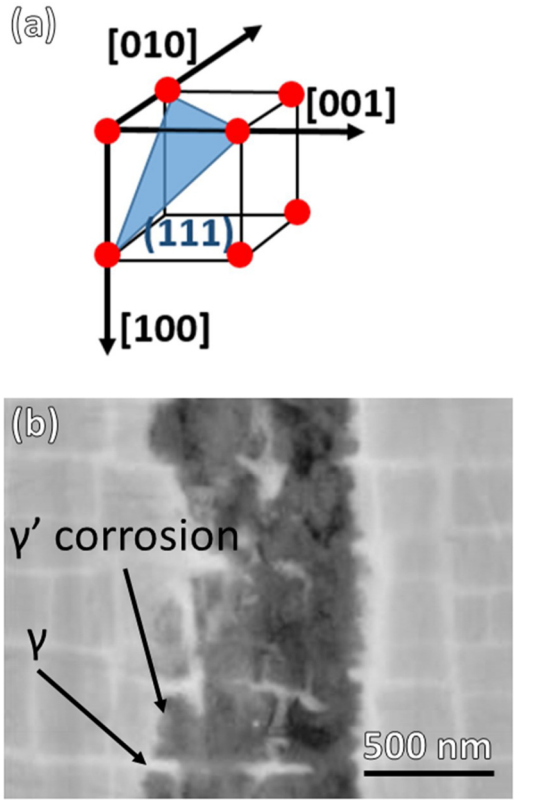

Fig. 2. (a) General crystallographic alignment for SEM/TEM images presented (b) Back scattered SEM image showing < 100 > crack propagation with preferential gamma-prime corrosion attack.

3. Results and discussion

Cracking was observed exclusively on the specimen surface exposed to tensile loading. SEM imaging of the cracked cross section of the specimen is presented in Fig. 2. Crack propagation on the cube planes can be seen, with corrosion preferentially interacting with the γ′ precipitates around the crack tip region. Comparison of corrosion occurring under tensile load (Fig. 3) with that occurring on the same specimen under compressive load (Fig. 4), shows a preference for corrosion to attack the γ′ precipitates under tension and γ channels under compression. This implies there could be a stress related effect is influencing the preference of the corrosion to attack either γ′/γ.

High magnification TEM imaging of the γ/γ′ interface confirmed

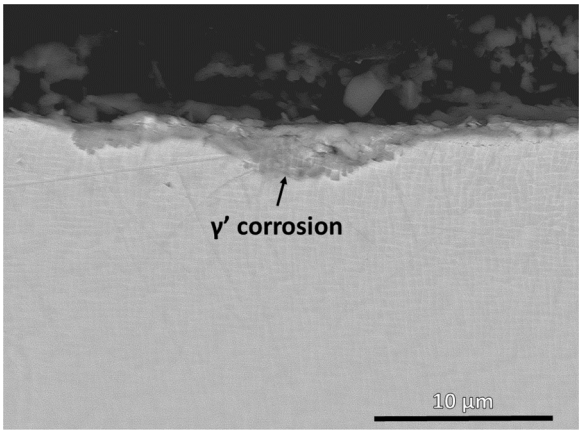

Fig. 3. Back scattered SEM image showing corrosion attack under tensile load with preferential gamma-prime attack.

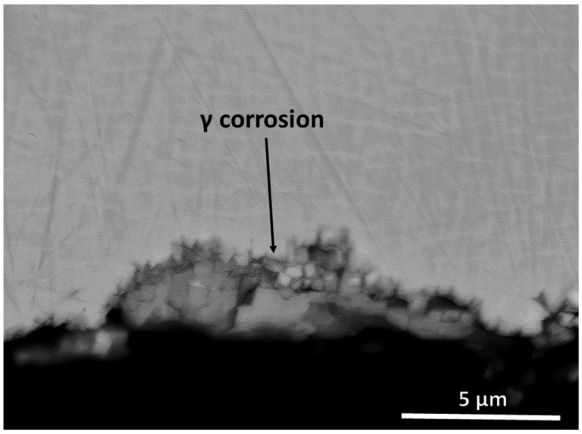

Fig. 4. Back scattered SEM image showing corrosion attack under compressive load with preferential gamma attack.

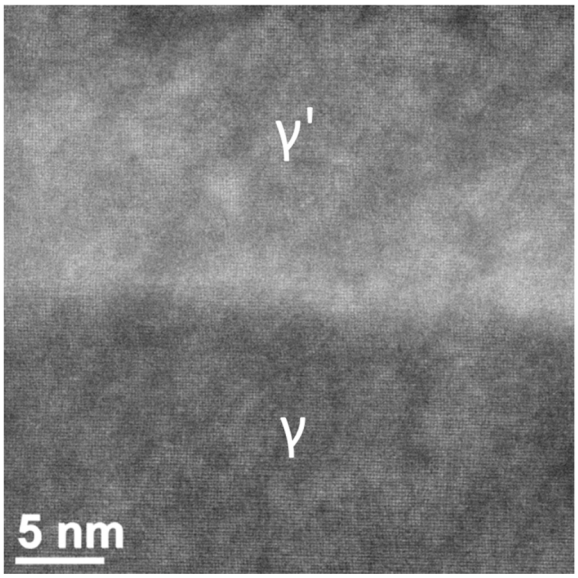

Fig. 5. Dark-field TEM image of gamma/gamma-prime interface showing good lattice coherence between the phases.

crystallographic coherence between the two phases (Fig. 5) at room temperature. Imaging of the crack tip (Fig. 6) showed cracks cutting through γ′ precipitates and propagating on the cube planes. Ahead of the crack tip, localised {111} slip traces/stacking faults were visible in γ′. These crystal defects were local to the crack tip, however, and do not appear to have influenced the propagation path of the crack in previous crack growth, as remnants of other faults were not found along the path of the crack.

A fracture ahead of the crack tip was also visible (Fig. 6a), this is most likely associated with an out of plane crack not fully visible in the TEM lamella. EDX mapping conducted in the STEM at the crack tip (Fig. 7) shows the presence of Na, and small concentrations of S indicating the corrosive atmosphere had penetrated to the crack tip. It can also be noted that the corrosive atmosphere at the crack tip appears to facilitate oxidation with oxide growth at the crack tip visible. No evidence of diffusion or absorption of corrosive elements can be seen ahead of the crack tip in the EDX mapping that was conducted, nor does the crack appear to interact with the crystallographic slip defects visible ahead of the crack tip. It is therefore suggested that corrosion enhanced de-cohesion or corrosion enabled reduction in fracture energy locally at the crack tip, is the more likely mechanism resulting in crack advancement and propagation.

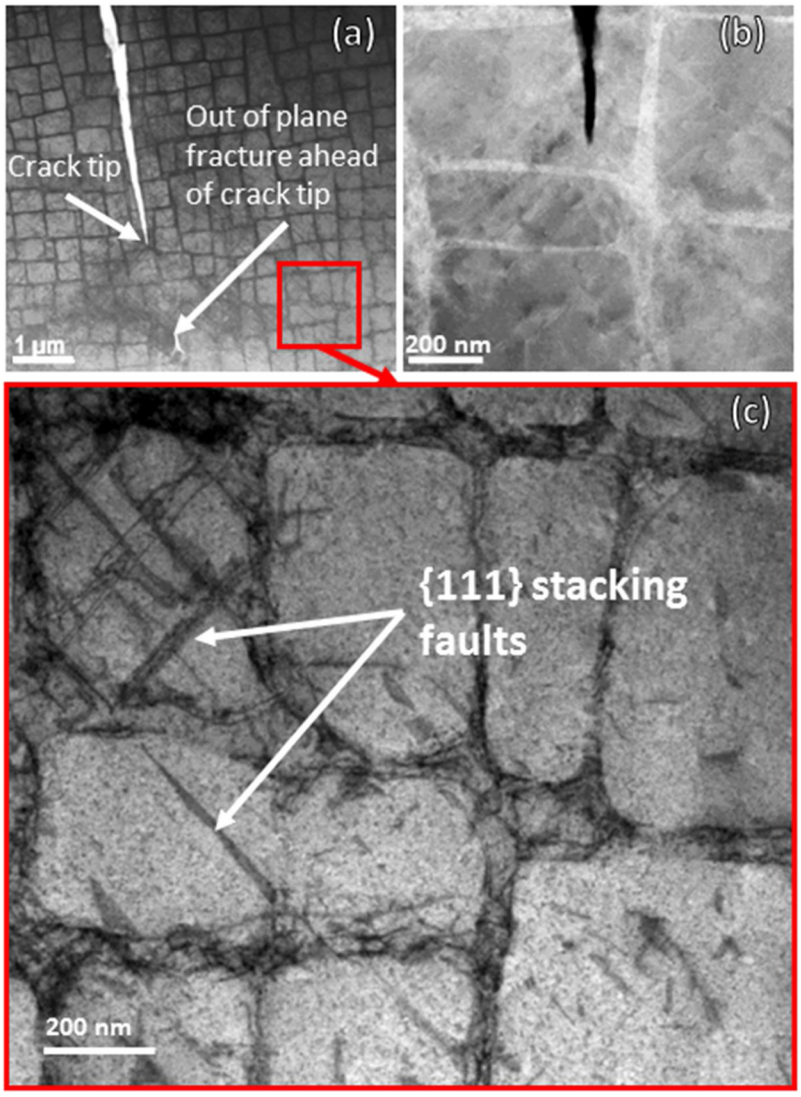

Fig. 6. (a) STEM image of the crack tip showing defect contrast (b) High angle annular dark field STEM image of crack tip (c) Higher magnification STEM image from the location shown in image (a) ahead of the crack tip, showing stacking defects or slip traces in the gamma-prime on {111} planes.

Fig. 7 appears to show strong segregation of elements between the γ and γ′ phases, with a higher concentration of Cr, Co and Mo in the γ channels, and a higher concentration of Ni, Al, Si, Ti and Ta in the γ′ precipitates. However, elemental maps such as these need to be analysed with care, since overlapping peaks in the EDX spectra can lead to anomalous results in the elemental maps, if not taken into account. Overlapping or adjacent peaks for O and Cr, Si and W, S and Mo, and Ni and Ta, for example, should all be borne in mind. All the segregation effects noted above do seem to accord with previously published EPMA, STEM and APT results on this alloy. The exceptions are W, Ta and Al, which show segregation gradients towards the γ′/ γ interfaces, but within the γ′ precipitates. For SC superalloys, such as CMSX-4, the γ′ phase contains Ti, Al and Ta; whilst the γ typically contains Mo, Co, Cr and Re [51,52]. However, W and Ir (if present) are reported to be nearly equally distributed between the γ/ γ' phases with Ni having a slight tendency to enrich the γ' [53].

The starting point for any discussion about segregation between the γ and γ′ phases is the Ni-Al phase diagram [54]. This shows that although Al is soluble in a Ni matrix, the solubility decreases markedly as the temperature is reduced. However, even at 400 °C, a Ni solid solution can absorb about 8 at% of Al before the ordered γ′ phase is formed. To a first approximation, this can be understood when the sizes of the respective elements are considered. Table 1 lists the Goldschmidt radii of the most common elements in CMSX-4 [55]. In particular the table shows that Al is much larger than Ni; hence as the composition of the alloy becomes richer in Al, the ordered γ′ phase is preferred, since this keeps the Al atoms as far apart as possible in a face centred cubic lattice. The sizes of Cr and Co are also similar to that of Ni and as such they tend to sit on the Ni sites in the γ or γ′ phases. In the specific case of CMSX-4, they tend to segregate primarily to the γ phase. On the other hand, the refractory elements such as Mo, W and Ta have much larger radii than Ni and hence might be expected to substitute for Al in the γ′ structure. Indeed Ta, with a similar radius to Al does indeed segregate strongly to the aluminium sites in the γ′ structure [56]. The situation for Mo and W is less clear cut, with Mo reported to segregate to the γ phase in a Ni-Al-Mo ternary alloy [57]. First-principles calculations by the same authors, however, do suggest that when Mo is present in the γ′ structure, it would substitute preferentially on the Al sub-lattice.

The partitioning between γ and γ′ is often described by a partitioning ratio $K_i^{\gamma'/\gamma}$, which is defined as the ratio of the concentration of element *i* in the γ′ precipitate to its concentration in the γ matrix. Hence in the case of Ta, for example, $K_{Ta}^{\gamma'/\gamma} > > 1$. The partitioning of W is more complex. In a quaternary Ni-Al-Cr-W alloy, for example, it has been reported [58] that there was twice as much W found in the γ′ phase as the γ phase. However, Amouyal et al [59] showed that partitioning of W is strongly influenced by the presence of Ta in a Ni based

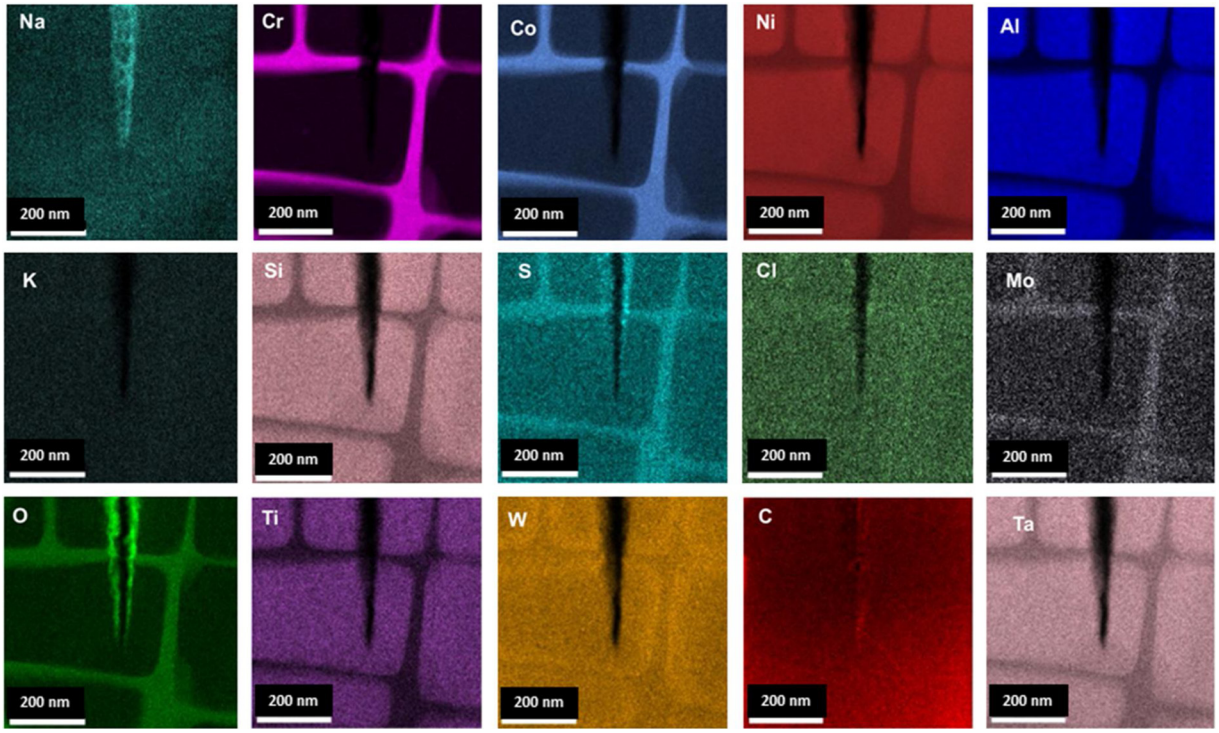

Fig. 7. STEM EDX mapping showing elemental segragation between the bulk γ′/ γ and the crack tip post-exposure.

Table 1
Goldschmidt atomic radii (in nm) of the main elements in CMSX-4 [61].

Ni	0.125
Al	**0.143**
Co	**0.126**
Cr	**0.128**
Ta	**0.147**
W	**0.141**
Re	**0.138**
Ti	**0.147**
Mo	**0.140**

superalloy. Hence, for example, in a ternary Ni-Al-W alloy, W segregates to the γ′ phase with $K_W^{\gamma'/\gamma} = 1.4$ but in a multicomponent alloy containing 1 at% Ta the W segregates to γ with $K_{Ta}^{\gamma'/\gamma} = 0.92$. Ta is such a strong γ′ segregant that its presence leads to site competition between the Ta and W. Indeed, Thermo-Calc calculations by Amouyal et al [60] suggest that the value of $K_W^{\gamma'/\gamma}$ decreases with increasing Ta concentration with a cross-over ($K_W^{\gamma'/\gamma} > 1$ to $K_W^{\gamma'/\gamma} < 1$) for a Ta concentration of 2 at% at 800 °C. In an alloy such as CMSX-4, which contains additions of Mo and Re as well as W and Ta, all the interactions between the different components may need to be considered. However, our results would appear to show that the W/Ta and W/Al interactions are the most dominant. Ta does segregate very strongly to the γ′ phase in CMSX-4 but there also appears to be an inverse correlation between the Ta concentration and the concentration of W near the edges of the γ′ precipitates. The W concentration is similar at the centre of the γ and γ′ regions, but the W signal rises strongly within the γ′ as the edges of the precipitates are approached. It then falls sharply at the γ/γ′ interface. The Ta and Al concentrations are very high at the centre of the γ′ precipitates but drop near the edges of the γ′ as the W signal increases, as shown in the line profiles in Fig. 8. The distance over which these changes are observed is several nm – too wide for beam broadening or instrumental broadening effects due to the proximity of the interface – and are not mirrored in the Cr or Re profile, for example. Hence there must be another explanation for the change in W segregation near the edges of the γ′ regions. Since the change extends over several nm, it is unlikely to be due to electronic structure changes associated with the γ/γ′ interface, which are usually confined to first or second nearest neighbours [60]. A more likely explanation is the influence of strain on the segregation profile. It has been shown, for example, that variations in Mo concentration can have a major influence on lattice misfit and creep resistance of multicomponent alloys, although there was no evidence of Mo segregation at the γ/ γ′ interface [61,62].

It has been reported that the misfit parameter, δ, given by $\delta = 2(a_{\gamma'} - a_{\gamma})/(a_{\gamma'} + a_{\gamma})$, where $a_{\gamma'}$ and a_{γ} are the lattice parameters of the γ′ phase and the γ matrix respectively [63], should have a positive value at both low and high temperatures, but decrease in magnitude at high temperatures, to achieve optimum creep performance [64]. In order to minimise any major interface strain, the segregation of W from the γ matrix into the γ′ zone may occur, either during high temperature heat treatment – a steady state condition – or in a more transitory way, as the sample is cooled. Given the low diffusivity of W in a Ni matrix compared to other substitutional elements [65], the former explanation seems more likely. The presence of a W gradient within the γ′ phase prior to testing at 550 °C would appear to reinforce that view.

Further EDX mapping of the fracture feature visible ahead of the crack tip in Fig. 6 is presented in Fig. 9. It can be concluded that the feature has been exposed to the corrosive environment as it contains environmental contaminants Na, O and S. This supports the hypothesis that the feature is a section of an out of plane crack rather that an internal defect. The feature also contains a small amount of Cl, the presence of which is most likely explained by contamination in the Na/K sulphate compound used for the deposit during testing. However, its presence at the crack tip suggests that chlorides could be significant in regards to load and LTHC interaction mechanisms, and further chloride based salts should be considered in future research.

Due to the static loading condition, it is clear that crack advancement is enabled by the local environment and conditions at the crack tip under combined loading and LTHC.

Stress/strain effects on the electrochemical potential or mechanical-

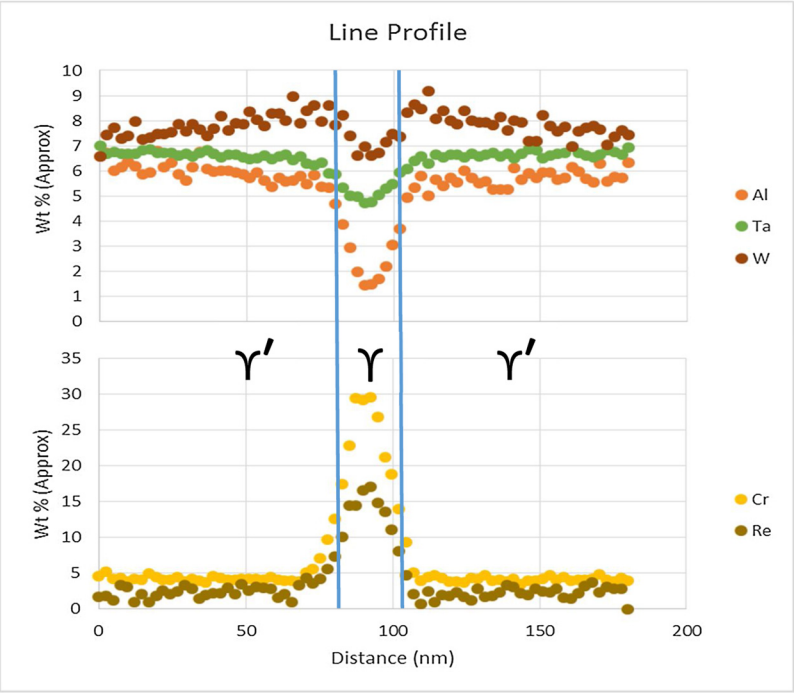

Fig. 8. Line profiles for Al, Ta, W, Cr and Re across a γ′/γ/γ′ interface showing the build-up of W near the edge of the γ′ particles and the corresponding reduction in Ta and Al.

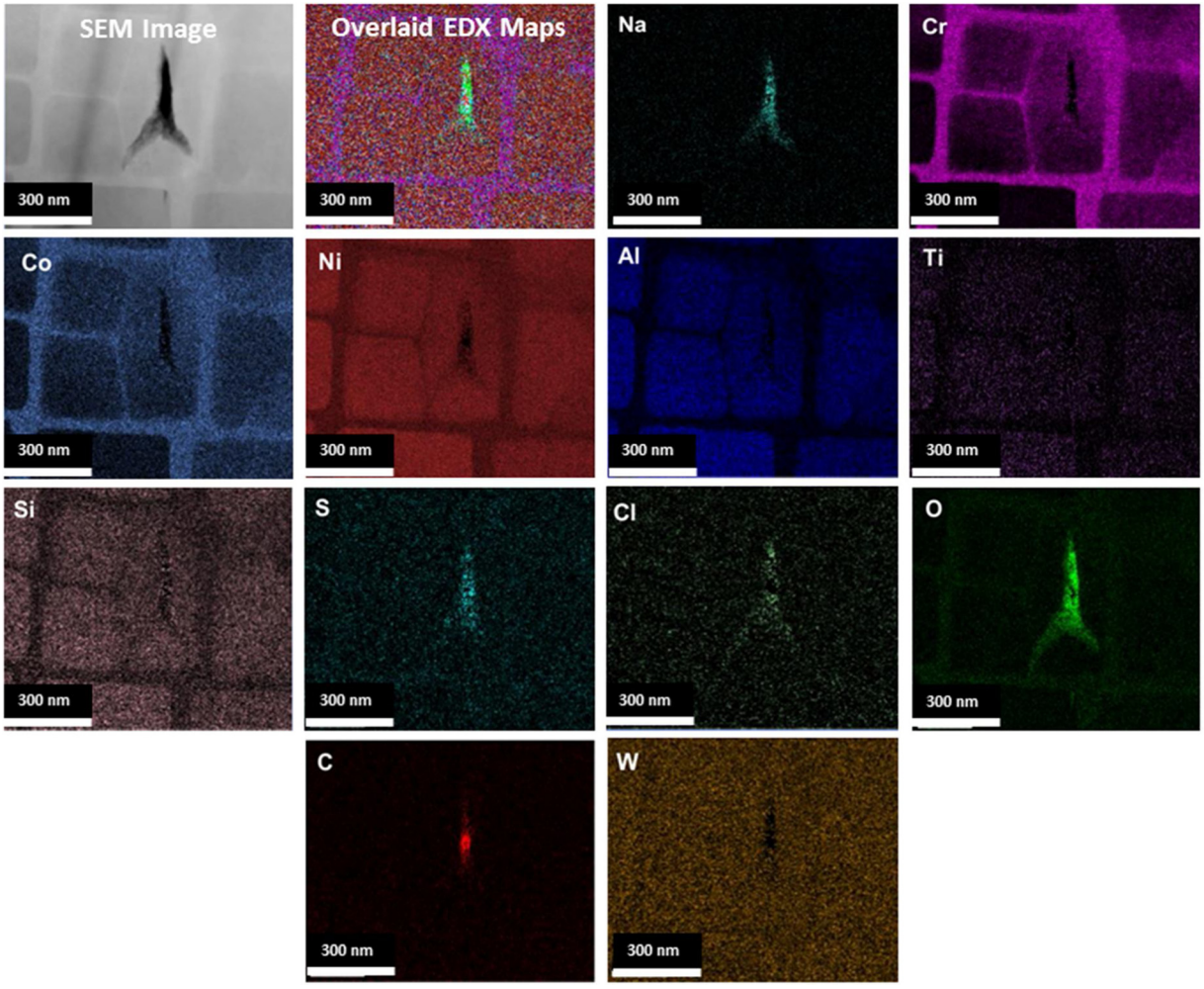

Fig. 9. STEM EDX mapping of feature ahead of the crack tip containing environmental elements, determined to be related to an out of plane crack.

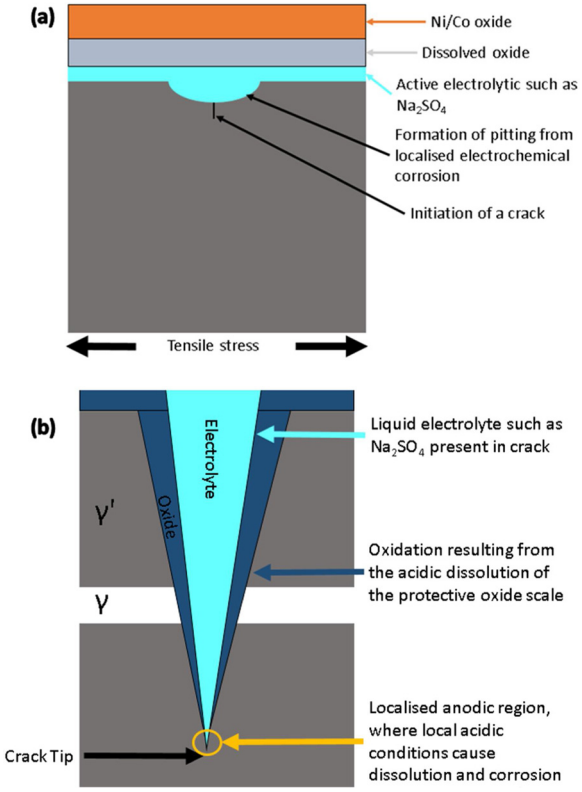

Fig. 10. Proposed mechanism of electrochemical corrosion generating LTHC stress corrosion cracking (a) Stage 1 where LTHC initiates and small pits start to form (b) Stage 2 where a crack has propagated and electrochemical corrosion is established at the crack tip.

chemical interactions have been observed and reported in crystalline materials [66,67], where it was demonstrated that increased tensile deformation can result in an increase in the anodic potential of the material and result in accelerated corrosion rates.

Following the deduction that an electrochemical corrosion mechanism is plausible at the crack tip, mechanical-chemical effects in the γ/ γ′ microstructure provide an explanation for the strain influenced preference of corrosion attack of the phases independently. Where the local strain conditions of the phases affects their anodic potential to a differing extent. Further experimental studies of stress effects on the preferential LTHC attack of the SC γ/ γ′ microstructure would help to further evidence this explanation.

A schematic of the proposed localised electrochemical hot corrosion cracking mechanism at the crack tip is presented in Fig. 10. The mechanism is comparable with other similar and more widely understood forms of electrochemical SCC [68][19], and draws on understanding gained from literature on the electrochemical nature of LTHC. The proposed LTHC cracking mechanism is evidenced by the finding of Na in the crack, determined through EDX analysis. The presence of Na in the crack is suggestive to there being a liquid melt likely containing Na_2SO_4 present under higher temperature LTHC test conditions. This is because the Na was likely to have been in liquid solution in order to have been able to migrate from the specimen surface to the crack tip at the test temperature of 550 °C. This is consistent with the expected chemistries of the liquid deposits formed in LTHC. The presence of a liquid electrolyte within a crack which was generated without any fatigue cycling, is strong evidence of an electrochemical SCC mechanism.

4. Conclusions

A form of high temperature hot corrosion SCC has been studied in a SC superalloy. Crack initiation and advancement was dependant on the simultaneous occurrence of LTHC and loading. The presence of Na within the crack, suggests that liquid electrolyte containing Na_2SO_4 is present at higher temperatures under LTHC conditions. A LTHC cracking mechanism has been proposed which was informed by both the experimental work and analysis presented, and review of relevant literature.

It is proposed that deformation of the γ/ γ′ could result in mechanical-chemical interactions effecting the chemical potential of the microstructural phases and resulting in preferential corrosion attack under different loading conditions, as were observed under compression and tension experimentally.

Detailed EDX mapping found that tungsten segregated close to the γ/ γ′ interface, but was concentrated in the γ′ in this alloy contrary to common historical understanding, an explanation of W occupying Ta or Al sites on the edges of the γ′ has been discussed. The impact of W and elemental segregation within the microstructure of SC superalloys, on the performance and specifically the corrosion performance of superalloys is not well understood and has therefore not been discussed. However elemental segregation within SC superalloys continues to be an important area of research for their continued development.

Acknowledgements

The authors acknowledge the support of the Engineering and Physical Research Council (EPSRC) for their support for the project - Flexible and Efficient Power Plant: Flex-E-Plant (Grant number: EP/K021095/1). They also thank the following partners for their the valuable contributions: GE Energy, Doosan Babcock Limited, Centrica plc., EDF Energy (West Burton Power) Limited., Uniper Technology Limited, Goodwin Steel Castings Limited, NPL Management Limited, R-MC Power Recovery Limited., RWE Generation UK plc., Scottish and Southern Energy (SSE) plc., Siemens Industrial Turbomachinery, and TWI Limited. Data underlying this study can be accessed through the Cranfield University repository at https://doi.org/10.17862/cranfield.rd.10033019.

References

[1] P.E. Sikorska, The need for legal regulation of global emissions from the aviation industry in the context of emerging aerospace vehicles, Int. Comp. Jurisprud. 1 (2) (2015) 133–142.
[2] UK Department of Energy and Climate Change, Updated energy and emissions projections 2013, Energy White Pap. 947 (November) (2008) 1–51.
[3] UNFCCC, Paris agreement, Conf. Parties Its Twenty-First Sess. (2015) 32 no. December.
[4] K. Tsukagoshi, J. Masada, A. Muyama, Y. Iwasaki, E. Ito, Operating status of uprating gas turbines and future trend of gas turbine development, Mitsubishi Heavy Ind. Ltd. Tech. Rev. 44 (4) (2007) 1–6.
[5] L. Brooking, J. Sumner, S. Gray, J.R. Nicholls, G. Marchant, N.J. Simms, Effect of stress state and simultaneous hot corrosion on the crack propagation and fatigue life of single crystal superalloy CMSX-4, Int. J. Fatigue (2018).
[6] H. Rosier, K. Perkins, A. Girling, J. Leggett, G. Gibson, Factors affecting the corrosion fatigue life in nickel based superalloys for disc applications, MATEC Web Conf. 14 (2014) 03001.
[7] L. Brooking, J. Sumner, S. Gray, N.J. Simms, Stress corrosion of Ni-based superalloys, Mater. High Temp. 35 (December) (2017) 120–129.
[8] R. Hashizume, A. Yoshinari, T. Kiyono, M. Morinaga, Development of Ni-Based single crystal superalloys for power-generation gas turbines, Superalloys 2004 (Tenth Int. Symp. (2004) 53–62.
[9] R.C. Reed, The superalloys, fundamentals and applications, The Superalloys, (2006) p. various.
[10] H.L. Cockings, K.M. Perkins, M. Dowd, Influence of environmental factors on the corrosion-fatigue response of a nickel-based superalloy, Mater. Sci. Technol. (United Kingdom) 33 (9) (2017) 1048–1055.
[11] G.S. Mahobia, N. Paulose, S.L. Mannan, R.G. Sudhakar, K. Chattopadhyay, N.C. Santhi Srinivas, V. Singh, Effect of hot corrosion on low cycle fatigue behavior of superalloy IN718, Int. J. Fatigue 59 (2014) 272–281.
[12] N. Chapman, L. Brooking, J. Sumner, S. Gray, J. Nicholls, Corrosion fatigue testing: the combined effect of stress and high temperature corrosion, Mater. High Temp. 35 (1–3) (2018).
[13] K.S. Chan, M.P. Enright, J.P. Moody, Development of a probabilistic methodology for predicting hot corrosion fatigue crack growth life of gas turbine engine disks, J. Eng. Gas Turbines Power 136 (2) (2014) 022505.
[14] T.P. Gabb, J. Telesman, B. Hazel, D.P. Mourer, The effects of hot corrosion pits on

the fatigue resistance of a disk superalloy, J. Mater. Eng. Perform. 19 (1) (2010) 77–89.
[15] D.J. Child, J. Meldrum, P. Onwuarolu, Corrosion-fatigue testing of Ni-based superalloy RR1000, Mater. Sci. Technol. (United Kingdom) 33 (9) (2017) 1040–1047.
[16] R.N. Parkins, third ed., Mechanisms of Stress-Corrosion Cracking vol. 1, Corros, 2013 no. Ref 1, p. 8:3-8:31.
[17] J.R. Donahue, A.B. Lass, J.T. Burns, The interaction of corrosion fatigue and stress-corrosion cracking in a precipitation-hardened martensitic stainless steel, NPJ Mater. Degrad. 1 (1) (2017) 11.
[18] N.S. Zadorozne, M.C. Giordano, A.E. Ares, R.M. Carranza, R.B. Rebak, Anodic characteristics and stress corrosion cracking behavior of nickel rich alloys in bicarbonate and buffer solutions, Corros. Sci. 108 (2016) 1–10.
[19] L.G. Bland, J.S. Locke, Chemical and electrochemical conditions within stress corrosion and corrosion fatigue cracks, NPJ Mater. Degrad. 1 (1) (2017) 12.
[20] L.J. Qiao, K.W. Gao, A.A. Volinsky, X.Y. Li, Discontinuous surface cracks during stress corrosion cracking of stainless steel single crystal, Corros. Sci. 53 (11) (2011) 3509–3514.
[21] M. Ahlers, E. Riecke, Stress corrosion cracking in single crystals of Fe-25Cr-20Ni, Corros. Sci. 18 (1) (1978) 21–38.
[22] E.I. Meletis, R.F. Hochman, The crystallography of stress corrosion cracking in face centered cubic single crystals, Corros. Sci. 24 (10) (1984) 843–862.
[23] W. Carpenter, B.S.-J. Kang, K.M. Chang, SAGBO mechanism on high temperature of Ni-base superalloys cracking behavior, Miner. Met. Mater. Soc. (1997) 679–688.
[24] X. Liu, L. Ma, K. Chang, Time-dependent crack growth behaviors of five superalloys, Miner. Met. Mater. Soc. (2001) 543–552.
[25] A.A.N. Németh, D.J. Crudden, D.E.J. Armstrong, D.M. Collins, K. Li, A.J. Wilkinson, C.R.M. Grovenor, R.C. Reed, Environmentally-assisted grain boundary attack as a mechanism of embrittlement in a nickel-based superalloy, Acta Mater. 126 (2017) 361–371.
[26] M. Gao, D.J. Dwyer, R.P. Wei, Chemical and microstructural aspects of creep crack growth in inconel 718 alloy, Superalloys 718 (625) (1994) 581–592 706 Var. Deriv..
[27] D.A. Woodford, Gas phase embrittlement and time dependent cracking of nickel based superalloys, Energy Mater. 1 (1) (2006) 59–79.
[28] J.P. Beckman, D.A. Woodford, Gas phase embrittlement of nickel by sulfur, Metall. Trans. A 21 (12) (1990) 3049–3061.
[29] M.C. Rezende, L.S. Araujo, S.B. Gabriel, D.S. dos Santos, L.H. de Almeida, Hydrogen embrittlement in nickel-based superalloy 718: relationship between g′ þ g 00 precipitation and the fracture mode, Int. J. Hydrogen Energy 40 (47) (2015) 17075–17083.
[30] P.D. Hicks, C.J. Altstetter, Comparison of internal hydrogen embrittlement of superalloys 718 and 625, Superalloys 718 (1991) 635–651 625 Var. Deriv..
[31] Z. Ahmad, Types of corrosion: materials and environments, Principles of Corrosion Engineering and Corrosion Control, (2006), pp. 120–270.
[32] C. Duret-Thual, Understanding corrosion: basic principles, Understanding Biocorrosion: Fundamentals and Applications, (2014), pp. 3–32.
[33] S. Lynch, Progress towards understanding mechanisms of hydrogen embrittlement and stress corrosion cracking, NACE Int. Corros. Conf., No. 07493 (2007) 1–29.
[34] H.K. Birnbaum, Mechanisms of Hydrogen Related Fracture of Metals, (1989).
[35] J. Li, A. Oudriss, A. Metsue, J. Bouhattate, X. Feaugas, Anisotropy of hydrogen diffusion in nickel single crystals: the effects of self-stress and hydrogen concentration on diffusion, Sci. Rep. 7 (February) (2017) 1–9.
[36] H. Vehoff, W. Rothe, Overview in gaseous hydrogen embrittlement FeSi- and Ni-single crystals, Acta Metall. 31 (11) (1983) 1781–1793.
[37] B.A. Pint, S. Dryepondt, K.A. Unocic, Oxidation of superalloys in extreme environments, 7th Int. Symp. Superalloy 718 Deriv. (2010) 861–875.
[38] A. Zahs, M. Spiegel, H.J. Grabke, Chloridation and oxidation of iron, chromium, nickel and their alloys in chloridizing and oxidizing atmospheres at 400-700°C, Corros. Sci. 42 (2000) 1093–1122.
[39] K.L. Luthra, O.H. LeBlanc, Low Temperature Hot Corrosion of Co-Cr-AI Alloys*, Mater. Sci. Eng. 87 (1987) 329–335.
[40] V. Mannava, A.S. Rao, N. Paulose, M. Kamaraj, R.S. Kottada, Hot corrosion studies on Ni-base superalloy at 650 °C under marine-like environment conditions using three salt mixture (Na2SO4 + NaCl + NaVO3), Corros. Sci. 105 (2016) 109–119.
[41] F.S. Pettit, G.H. Meier, Oxidation and Hot Corrosion of Superalloys, Superalloys 1984 (Fifth International Symposium) (1984) 651–687.
[42] N. Birks, G.H. Meier, F.S. Pettit, High-temperature corrosion resistance, JOM 39 (12) (1987) 28–31.
[43] N. Eliaz, G. Shemesh, R.M. Latanision, Hot corrosion in gas turbine components, Eng. Fail. Anal. 9 (1) (2002) 31–43.
[44] D.A. Shifler, Hot corrosion: a modification of reactants causing degradation, Mater. High Temp 5 (1–3) (2018) 225–235.
[45] P. Lortrakul, R.W. Trice, K.P. Trumble, M.A. Dayananda, Investigation of the mechanisms of Type-II hot corrosion of superalloy CMSX-4, Corros. Sci. 80 (2014) 408–415.
[46] R.A. Rapp, Chemistry and electrochemistry of hot corrosion of metals, Mater. Sci. Eng. 87 (C) (1987) 319–327.
[47] W. Gao, Z. Li, Developments in High-temperature Corrosion and Protection of Materials, (2008).
[48] (ASM International), Hot Corrosion in Gas Turbines, High Temp. Corros. Mater. Appl., 2007, pp. 249–258.
[49] British Standards Institutions, "BSI Standards Publication Plastics — Determination of Flexural Properties, (2013).
[50] J. Sumner, A. Encinas-Oropesa, N. Simms, J.R. Nicholls, Type II hot corrosion: behaviour of CMSX-4 and IN738LC as a function of corrosion environment, Mater. Corros (2) (2014) 188–196.
[51] A.B. Parsa, P. Wollgramm, H. Buck, C. Somsen, A. Kostka, I. Povstugar, P.P. Choi, D. Raabe, A. Dlouhy, J. Müller, E. Spiecker, K. Demtroder, J. Schreuer, K. Neuking, G. Eggeler, Advanced scale bridging microstructure analysis of single crystal Ni-base superalloys, Adv. Eng. Mater. 17 (2) (2015) 216–230.
[52] B. Dubiel, P. Indyka, I. Kalemba-Rec, T. Moskalewicz, Analytical Electron microscopy studies of the CMSX-4 single crystal superalloy subjected to high temperature annealing, Acta Phys. Pol. A 131 (5) (2017) 1375–1379.
[53] F. Pyczak, B. Devirent, H. Mughrabi, The Effects of Different Alloying Elements on the Thermal Expansion Coefficients, Lattice Constants and Misfit of Nickel-Based Superalloys Investigated by X-Ray Diffraction, Superalloys 2004 (2004) 827–836. Tenth Int. Symp..
[54] J.M. Sanchez, J.R. Barefoot, R.N. Jarrett, J.K. Tien, Modeling of γ/γ′ phase equilibrium in the nickel-aluminum system, Acta Metall. 32 (September 9) (1984) 1519–1525.
[55] E.A. Brandes, G.B. Brook, Smithells Metals Reference Book, 7th ed., (1992).
[56] C. Booth-Morrison, Z. Mao, R.D. Noebe, D.N. Seidman, Chromium and tantalum site substitution patterns in Ni3 Al (L 12) γ′ -precipitates, Appl. Phys. Lett. 93 (3) (2008) 1–4.
[57] Y. Tu, Z. Mao, D.N. Seidman, Phase-partitioning and site-substitution patterns of molybdenum in a model Ni-Al-Mo superalloy: An atom-probe tomographic and first-principles study, Appl. Phys. Lett. 101 (12) (2012).
[58] C.K. Sudbrack, T.D. Ziebell, R.D. Noebe, D.N. Seidman, Effects of a tungsten addition on the morphological evolution, spatial correlations and temporal evolution of a model Ni-Al-Cr superalloy, Acta Mater. 56 (3) (2008) 448–463.
[59] Y. Amouyal, Z. Mao, C. Booth-Morrison, D.N. Seidman, On the interplay between tungsten and tantalum atoms in Ni-based superalloys: an atom-probe tomographic and first-principles study, Appl. Phys. Lett. 94 (4) (2009).
[60] Y. Amouyal, Z. Mao, D.N. Seidman, Effects of tantalum on the partitioning of tungsten between the γ- and γ′-phases in nickel-based superalloys: linking experimental and computational approaches, Acta Mater. 58 (18) (2010) 5898–5911.
[61] R.A. MacKay, M.V. Nathal, D.D. Pearson, Influence of molybdenum on the creep properties of nickel-base superalloy single crystals, Metall. Trans. A 21 (1) (1990) 381–388.
[62] R. Jayaram, J.J. Hren, M.K. Miller, APFIM/TEM characterization of solute partitioning in a model Ni-Mo-Al-Ta superalloy, Surf. Sci. 246 (1–3) (1991) 323–328. Apr.
[63] H. Mughrabi, U. Tetzlaff, Microstructure and high-temperature strength of monocrystalline nickel-base superalloys, Adv. Eng. Mater. 2 (6) (2000) 319–326.
[64] J. Svoboda, P. Lukáš, Model of creep in 〈001〉-oriented superalloy single crystals, Acta Mater. 46 (10) (1998) 3421–3431.
[65] A.K. Jena, M.C. Chaturvedi, The role of alloying elements in the design of nickel-base superalloys, J. Mater. Sci. 19 (10) (1984) 3121–3139.
[66] F. Farhad, X. Zhang, D. Smyth-Boyle, Fatigue behaviour of corrosion pits in X65 steel pipelines, Proc. Inst. Mech. Eng. Part C J. Mech. Eng. Sci. (2018) 1–12 vol. 0, no. 0.
[67] E.M. Gutman, G. Solovioff, D. Eliezer, The mechanochemical behavior of type 316L stainless steel, Corros. Sci. 38 (July 7) (1996) 1141–1145.
[68] D.D. Macdonald, The electrochemical nature of stress corrosion cracking, Stress Corros. Crack. Nickel Based Alloy. Water-cooled Nucl. React, (2016), pp. 239–294 January.

2019-10-18

Analysis of combined static load and low temperature hot corrosion induced cracking in CMSX-4 at 550°C

Brooking, Laurie

Elsevier

Brooking L, Gray S, Dawson K, et al., (2020) Analysis of combined static load and low temperature hot corrosion induced cracking in CMSX-4 at 550°C. Corrosion Science, Volume 163, February 2020, Article number 108293

https://doi.org/10.1016/j.corsci.2019.108293